VNUHCM Journal of Science and Technology Development 2026, 29(3):4168-4173

Open Access Full Text Article

Research article

Energy dependence of secondary neutron equivalent dose from proton (70–250 MeV) therapy unit: Monte Carlo simulation

Huynh Thi Yen Hong[1,2,3,*], Truong Huu Ngan Thy[1,2,3], Vo Hong Hai[1,3], Trinh Hoa Lang[1,3]

ABSTRACT

Introduction: *The generation of secondary neutrons in proton therapy produces a biologically significant out-of-field dose, which is associated with an elevated risk of secondary cancers. This study was designed to quantify the absorbed and equivalent doses from these neutrons within a water phantom, specifically to establish how these doses depend on the initial energy of the proton beam.*

Methods: *We utilized a validated Monte Carlo model on the Geant4/GATE platform to simulate a pencil proton beam incident on a water phantom at energies ranging from 70 to 250 MeV. Model accuracy was verified by comparing the simulated Bragg peak positions (R_{80}) against NIST reference data. The secondary neutron absorbed dose was isolated using the DoseActor and Digitizer tools. Subsequently, the neutron equivalent dose (H) was calculated using energy-dependent radiation weighting factors (w_R), as recommended in ICRP Publication 103. All dose calculations were normalized to a clinically standard therapeutic dose of 2 Gy delivered to the Bragg peak.*

Results: *The simulations revealed a substantial increase in the neutron dose with increasing incident proton energy. As the proton energy was increased from 70 to 250 MeV, the mean neutron absorbed dose escalated from 0.031 to 0.138 mGy per 2 Gy therapeutic fraction. This caused the mean neutron equivalent dose to climb from 0.25 to 1.45 mSv. Furthermore, spatial analysis showed that the majority of this neutron dose is deposited in the entrance channel, upstream of the Bragg peak.*

Conclusion: *The secondary neutron equivalent dose delivered during proton therapy shows a strong dependence on treatment energy, with a nearly sixfold increase observed across the clinical energy range investigated. These quantitative findings are vital for clinicians and medical physicists in evaluating the risk-benefit ratio of treatments requiring high-energy proton beams and in developing more accurate algorithms for treatment planning systems.*

Key words: Pencil Beam Scanning, Geant4, GATE, Stray Radiation, Radiation Weighting Factor, Risk Assessment

[1]*Vietnam National University, Ho Chi Minh City, Vietnam*

[2]*Nuclear Technique Laboratory, University of Science, Ho Chi Minh City, Vietnam*

[3]*Faculty of Physics and Engineering Physics, University of Science, Ho Chi Minh City, Vietnam*

Correspondence

Huynh Thi Yen Hong, Vietnam National University, Ho Chi Minh City, Vietnam

Nuclear Technique Laboratory, University of Science, Ho Chi Minh City, Vietnam

Faculty of Physics and Engineering Physics, University of Science, Ho Chi Minh City, Vietnam

Email: htyhong@hcmus.edu.vn

History

- Received: 11-12-2025
- Revised: 02-02-2026
- Accepted: 02-03-2026
- Published Online: 10-07-2026

DOI : 10.32508/vnuhcmj-std.v29i3.4639

INTRODUCTION

Proton therapy represents a significant advance in radiation oncology, offering a distinct dosimetric advantage over conventional photon-based radiotherapy. This superiority stems from the characteristic Bragg peak, a physical phenomenon in which protons deposit the majority of their energy over a very narrow range at the end of their path, followed by a sharp, finite dose fall-off. This allows highly precise delivery of a therapeutic dose that conforms tightly to the tumor volume while maximally sparing surrounding tissues and organs at risk (OARs) distal to the target [1]. However, this therapeutic precision is inevitably accompanied by the production of a complex, mixed field of secondary radiation generated through inelastic nuclear interactions between the primary proton beam and the nuclei of the elements that comprise human tissue [2].

Among the various particles comprising this secondary field, neutrons are the primary clinical concern. Unlike charged secondary particles, which have a limited range, neutrons are uncharged; therefore, they are highly penetrating, allowing them to travel significant distances from the primary beam path and contribute to a whole-body, out-of-field dose [2]. Critically, neutrons have a high relative biological effectiveness (RBE), meaning they induce more complex and severe DNA damage per unit absorbed dose than photons or protons [3]. This elevated biological damage potential translates directly to an increased lifetime attributable risk (LAR) of developing secondary malignancies [4]. This risk is of particular gravity in pediatric oncology, where patients have both a long life expectancy for stochastic effects to manifest and an increased intrinsic radiosensitivity of developing tissues [5]. Recent studies have also highlighted the importance of assessing out-of-field doses for other sensitive groups, such as pregnant patients [6], and evaluating safety for parents accompanying children during treatment [7].

Cite this article : Thi Yen Hong H, Huu Ngan Thy T, Hong Hai V, Hoa Lang T. **Energy dependence of secondary neutron equivalent dose from proton (70–250 MeV) therapy unit: Monte Carlo simulation**. *VNUHCM J. Sci. Technol. Dev.* 2026; 29(3):4168-4173.

Consequently, the accurate quantification of the secondary neutron dose is indispensable for comprehensive risk assessment and treatment optimization. Extensive efforts have been made to characterize these secondary neutron fields through both measurements in proton therapy centers [8] and advanced Monte Carlo simulations comparing different ion species. While the physical yield of neutrons has been studied, translating this physical information into a clinically meaningful biological metric, the neutron equivalent dose (H_n), remains complex due to the continuous nature of neutron energy spectra. The equivalent dose accounts for the differential biological harm caused by different types of radiation and is calculated by multiplying the neutron absorbed dose (D_n) by an energy-dependent radiation weighting factor (w_R), as defined by the International Commission on Radiological Protection (ICRP). While commercial treatment planning systems (TPS) are highly optimized for target volume dose calculations, they often employ analytical algorithms that prioritize speed. These models may have limitations in accurately predicting far-out-of-field neutron doses compared with full Monte Carlo simulations, necessitating independent verification methods.

This study utilizes the Geant4/GATE platform to systematically investigate the relationship between the initial proton beam energy and the resulting secondary neutron dose equivalent. By leveraging Monte Carlo simulations, the gold standard for modeling coupled particle transport in radiotherapy [2], this work quantifies both the neutron absorbed dose (D_n) and the neutron equivalent dose (H_n) in a water phantom for proton energies ranging from 70 to 250 MeV. The objective is to provide a comprehensive, open-source dataset that can inform clinical risk-benefit analyses and serve as a supplementary benchmark for validating Monte Carlo configurations and refining treatment planning algorithms, contributing to the ongoing effort to precisely characterize secondary doses in proton therapy.

MATERIALS AND METHODS

Monte Carlo Simulation Model

Simulation Platform and Geometry

The study was conducted using the Geant4 Application for Tomographic Emission (GATE) simulation toolkit (version 9.0), which is built upon the robust Geant4 (version 10.7) libraries. GATE is a well-validated and widely used platform in medical physics, specifically designed to model radiotherapy scenarios with high accuracy. The simulation geometry consisted of a $27 \times 27 \times 57$ cm^3 water phantom, which is the standard reference medium for radiation dosimetry due to its tissue-equivalent properties. These dimensions were chosen to be large enough to provide full lateral electronic equilibrium and contain the entire range of the highest-energy proton beam, ensuring accurate scoring of the full dose distribution and secondary particle scatter.

Beam Configuration and Simulation Parameters

The phantom was irradiated with a monoenergetic pencil proton beam, representing the fundamental component of modern pencil beam scanning systems. Simulations were performed for five clinically relevant incident proton energies: 70, 100, 150, 200, and 250 MeV, covering the range from shallow to deep-seated tumor treatments. To achieve a low statistical uncertainty (<1%) in the dose calculations, 10^9 primary proton histories were simulated at each energy level.

Physics Model and Validation

Physics model selection is critical for accurately simulating the primary proton interactions and the subsequent transport of secondary particles. We employed the QGSP_BIC_HP_EMY physics list, which is a standard and recommended configuration for proton therapy applications. This composite list combines:

The quark-gluon string precompound (QGSP) model for high-energy hadronic interactions (>10 GeV).

The binary cascade (BIC) model for intermediate-energy hadronic interactions.

The high precision (HP) neutron model for tracking neutrons with energies below 20 MeV, which uses evaluated cross-section data from the ENDF/B-VII.1 library for high-fidelity transport.

The "EMY" standard electromagnetic physics option for accurate modeling of electron, positron, and photon interactions.

The accuracy of the primary proton beam transport was validated. The simulated depth-dose profiles for the primary protons were used to determine the proton range, defined as R_{80} (the depth of the 80% dose on the distal fall-off of the Bragg peak). These simulated R_{80} values were compared against the authoritative PSTAR database from the National Institute of Standards and Technology (NIST). Across all five energies, the deviation between our simulated ranges and the NIST reference data was less than 1.64%,

confirming the high accuracy of our electromagnetic physics model and geometric setup. Because electromagnetic interactions primarily determine R80, the validation of the hadronic physics model governing secondary neutron production is addressed in the discussion section by comparing it with previously published Monte Carlo data.

Neutron Dose Calculation

The three-dimensional dose distribution throughout the phantom was scored using a GATE DoseActor. A high spatial resolution was achieved by setting the voxel size to $1 \times 1 \times 1$ mm^3. To specifically isolate the dose contribution from secondary neutrons, we implemented a filtering strategy. The Digitizer module was used to record every energy-deposition event (a "hit") within the phantom. Each hit contains information about the particle that caused it. These hits were filtered, and only those created by particles with a particle data group (PDG) code of 2112, the unique identifier for the neutron, were retained. This process effectively removes the dose contributions from primary protons and all other secondary charged particles (e.g., electrons, secondary protons, and alphas).

Monte Carlo simulations calculate dose on a per-primary-particle basis. To translate these results into a clinically relevant context, all dose values were normalized. For each incident proton energy, a normalization factor was determined by calculating the number of primary protons required to deliver an absorbed dose of exactly 2 Gy to the Bragg peak maximum. This same normalization factor was then applied to the scored neutron dose distribution. The final mean absorbed neutron dose (D_n) was calculated over the entire phantom volume and is reported in units of mGy per 2 Gy therapeutic fraction.

The absorbed dose (D_n), measured in Grays (Gy), does not fully capture the biological impact of different types of radiation. To assess biological risk, the absorbed neutron dose was converted to the equivalent dose (H_n), a protection quantity measured in Sieverts (Sv). This conversion was performed using the energy-dependent radiation weighting factor (w_R) for neutrons, as defined in ICRP Publication 103. The w_R for neutrons is not a single value but a continuous function of the kinetic energy of the neutron.

To implement this, the neutron fluence spectrum (number of neutrons per unit area per unit energy) was scored and averaged over the entire phantom volume for each incident proton energy. The relative fluence values were normalized to the absolute fluence (cm^{-2}) based on the therapeutic dose. A single, spectrum-averaged radiation weighting factor ($w_{R,avg}$) was then calculated by convoluting this absolute fluence spectrum with the ICRP 103 $w_R(E_n)$ function. This approach simplifies the spatially varying neutron spectrum to a single average value and provides a robust, conservative estimate of the overall biological dose burden. The mean neutron equivalent dose (H_n) was then calculated using the formula:

$$H_n = D_n \times w_{Ravg}$$

where D_n is the mean neutron absorbed dose, and w_{Ravg} is the calculated average radiation weighting factor for the specific neutron spectrum generated by each primary proton energy.

RESULTS

Neutron Production Yield and Energy Spectrum

A significant by-product of non-elastic proton nuclear interactions is the generation of secondary neutrons. A strong, positive correlation was quantified between the incident proton energy and the neutron yield. As detailed in Table 1, the relative neutron yield, defined as the number of neutrons produced inside the phantom per incident proton, increased by more than 19-fold, from 1.78% at 70 MeV to 34.84% at 250 MeV, as the incident proton energy increased. This is a direct consequence of the larger cross-sections for non-elastic nuclear reactions at higher proton energies.

Table 1: Neutron production yield within a water phantom as a function of incident proton energy.

Incident Proton Energy (MeV)	Relative Yield (%)
70	1.78 ± 0.02
100	4.93 ± 0.05
150	12.94 ± 0.13
200	23.22 ± 0.23
250	34.84 ± 0.35

Note: Uncertainties represent one standard deviation (k=1).

Analysis of the neutron energy spectra revealed two key characteristics. First, neutrons produced inside the phantom exhibited a continuous energy distribution with a characteristic evaporation peak around 2 MeV, and a maximum energy close to the incident proton energy. Second, the spectra become progressively "harder" as the incident proton energy increased: they contained a greater proportion of high-energy neutrons.

The simulated neutron energy spectra are illustrated in Figure 1. The spectra revealed two distinct mechanisms of neutron production. First, a prominent evaporation peak was consistently observed around 2 MeV across all incident energies, originating from the de-excitation of compound nuclei. Second, a high-energy tail extended from the evaporation peak up to the maximum energy of the incident proton. As the proton energy increased from 70 to 250 MeV, this tail extended significantly, indicating a "spectral hardening" effect. This hardening is clinically significant because high-energy neutrons have different radiation weighting factors (w_R) than thermal or evaporation neutrons.

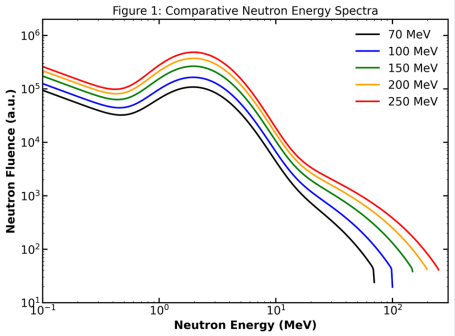

Figure 1: Comparative neutron fluence energy spectra within a water phantom for incident proton energies ranging from 70 to 250 MeV. The spectra are displayed on a log-log scale to highlight the characteristic evaporation peak around 2 MeV and the spectral hardening (high-energy tail) that increases with incident proton energy.

Yield and Directionality of Escaping Neutrons

A significant fraction of the neutrons produced within the phantom have sufficient energy to escape its boundaries, contributing to the out-of-field dose. Table 2 quantifies the total escaping neutron yield and its directional distribution relative to the beam axis. An analysis of the directionality reveals an important interplay between production kinematics and phantom geometry. As the incident proton energy increased, the initial production of secondary neutrons became kinematically forward-peaked due to momentum conservation. However, due to the elongated geometry of the phantom (57 cm long), these forward-directed neutrons had a high probability of undergoing scattering interactions within the water medium before reaching the distal face. Consequently, a substantial fraction of the neutrons were scattered and laterally escaped.

As shown in Table 2, at 250 MeV, although the forward yield (1.99%±0.02%) is higher than at 70 MeV (0.56%±0.01%), the lateral yield (17.29%±0.17%) remains the dominant component of the total escaping flux. While the primary interaction directed neutrons forward, the resulting out-of-field radiation field surrounding the phantom was substantial in all lateral directions, creating a diffuse "neutron bath" around the target volume.

Neutron Absorbed and Equivalent Dose

The ultimate clinical concern is the dose deposited by these neutrons. The substantial observed increase in neutron production (Table 1) directly translated to a higher mean absorbed dose (D_n), which rose by a factor of 4.5 from 70 to 250 MeV (Table 3).

To assess the biological risk, the absorbed dose was converted to equivalent dose (H_n). The "harder" neutron spectra at higher energies resulted in a larger spectrum-averaged radiation weighting factor (w_{Ravg}), which increased from 8.1 to 10.5. This synergy—more neutrons that are also more biologically effective—led to a steep, nearly six-fold increase in the mean neutron equivalent dose, which climbed from 0.25 mSv to 1.45 mSv per 2 Gy fraction. Spatial analysis confirmed that the highest dose concentration occurs in the entrance path, well upstream of the Bragg peak, creating a "neutron bath" that irradiates healthy tissue.

To visualize the spatial distribution of the secondary dose, Figure 2 presents a 2D dose map for the 150 MeV beam on a logarithmic scale. While the primary protons deposit their energy within a narrow path ending at the Bragg peak, a diffuse "neutron bath" is observed extending laterally and distally throughout the phantom. This confirms that healthy tissues located parallel to the beam path (lateral OARs) are subject to continuous low-dose exposure from scattered secondary neutrons, consistent with data on lateral neutron escape yields.

DISCUSSION

To validate the hadronic physics model (QGSP_BIC_HP) governing neutron production, our calculated neutron yields were compared with previously published Monte Carlo studies. For instance, at 250 MeV, the calculated relative yield of 34.84% is consistent with the findings of Griffin et al. (2022) (7), who reported comparable total neutron yields using the MCNP6 and PHITS codes for similar water phantom geometries. This agreement supports the reliability of our Geant4/GATE configuration for

Table 2: Yield and directional distribution of secondary neutrons escaping phantom relative to incident proton beam.

Incident Proton Energy (MeV)	Total Escaping Yield (%)	Forward Yield[1] (%)	Lateral Yield[2] (%)	Backward Yield[3] (%)
70	1.24 ± 0.01	0.56 ± 0.01	0.67 ± 0.01	0.01 ± 0.00
100	3.23 ± 0.03	1.03 ± 0.01	2.12 ± 0.02	0.08 ± 0.00
150	8.19 ± 0.08	1.59 ± 0.02	6.13 ± 0.06	0.47 ± 0.01
200	14.75 ± 0.15	1.85 ± 0.02	11.50 ± 0.12	1.38 ± 0.01
250	22.54 ± 0.23	1.99 ± 0.02	17.29 ± 0.17	3.26 ± 0.03

[1] *Forward: Neutrons exiting the distal face of the phantom.*
[2] *Lateral: Sum of neutrons exiting all four lateral sides of the phantom.*
[3] *Backward: Neutrons exiting the proximal (entrance) face of the phantom.*

Table 3: Calculated mean neutron absorbed dose (D_n) and equivalent dose (H_n) per 2 Gy therapeutic fraction as a function of incident proton energy.

Incident Proton Energy (MeV)	Mean Neutron Absorbed Dose, Dn (mGy/2 Gy)	Average Neutron wR	Mean Neutron Equivalent Dose, Hn (mSv/2 Gy)
70	0.031	8.1	0.25
100	0.054	8.8	0.48
150	0.091	9.5	0.86
200	0.120	10.1	1.21
250	0.138	10.5	1.45

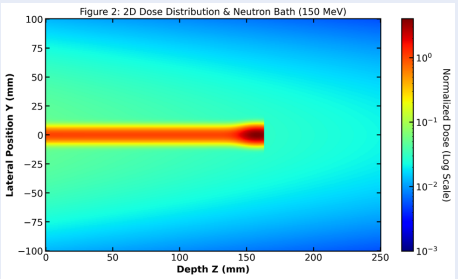

Figure 2: Two-dimensional dose distribution map (YZ plane) for a 150 MeV proton beam. The color scale is logarithmic to visualize the large dynamic range between the primary proton beam (red/orange) and the low-dose secondary neutron bath (cyan/green), which extends laterally into the phantom.

secondary particle transport. This study translates the physical characteristics of secondary neutrons, from their initial production (Table 1) to their transport and escape (Table 2) and ultimate biological impact (Table 3), into the clinically relevant metric of equivalent doses. Our key finding is a strong, positive correlation between incident proton energy and secondary neutron equivalent dose, which increases by nearly a factor of 6 across the clinical energy range. A clinician choosing to treat a deep-seated tumor (e.g., at a depth of 30 cm, requiring ~220 MeV protons) will subject the patient to an out-of-field neutron dose several times higher than that for a shallow tumor treatment (e.g., at 4 cm, requiring ~70 MeV protons).

The magnitude of the equivalent dose, reaching up to 1.45 mSv per 2 Gy fraction, is significant. For a typical 30-fraction course of treatment, the cumulative neutron equivalent dose could exceed 40 mSv. This level of whole-body exposure is a non-trivial factor in stochastic risk calculations, especially for pediatric patients with long life expectancies.

Our results provide quantitative data that can directly inform clinical decision-making. The finding that neutron production increases dramatically with energy (Table 1) provides quantitative evidence supporting the recommendation to use the lowest possible proton energy that can adequately cover the target volume. Furthermore, the data on escaping neutrons (Table 2) reveal a high lateral escape fraction (up to

~17% at 250 MeV). This suggests that careful attention should be paid to OARs located laterally to the target volume, in addition to those located distally. This comprehensive dataset can serve as a supplementary benchmark for developers of TPSs and for validating analytical dose algorithms, which may have uncertainties in estimating far-out-of-field neutron dose.

The primary limitation of this work is the use of a homogeneous water phantom. Future studies will extend this dose calculation methodology to patient-derived CT-based phantoms to investigate the influence of tissue heterogeneities (e.g., bone and lung) on neutron dose distribution in specific OARs. This methodology has been demonstrated effectively using age-dependent voxel phantoms.

CONCLUSIONS

This study successfully quantified the strong, positive correlation between incident proton energy and the secondary neutron equivalent dose in proton therapy. Using a validated Monte Carlo model, the neutron equivalent dose increases nearly sixfold across the clinical proton energy range of 70 to 250 MeV. This substantial increase underscores the clinical importance of accounting for the secondary neutron dose, particularly when high-energy beams are required to treat deep-seated tumors. This work provides a valuable quantitative foundation for the radiation oncology community, enabling more informed risk–benefit assessments and serving as a reference for refining next-generation treatment planning algorithms to better optimize the safety and efficacy of proton therapy.

LIST OF ABBREVIATIONS

GATE: Geant4 Application for Tomographic Emission

ICRP: International Commission on Radiological Protection

LAR: Lifetime Attributable Risk

NIST: National Institute of Standards and Technology

OARs: Organs at Risk

PDG: Particle Data Group

RBE: Relative Biological Effectiveness

TPS: Treatment Planning Systems

AUTHORS' CONTRIBUTIONS

Conceptualization and Methodology: H.T.Y. Hong, V.H. Hai.

Investigation and Data Curation: T.H.N. Thy, T.H. Lang.

Formal Analysis and Writing – Original Draft: H.T.Y. Hong.

Writing – Review & Editing: All authors contributed to the review and editing of the final manuscript.

Supervision: H.T.Y. Hong.

ACKNOWLEDGEMENTS

The authors would like to thank the reviewers. English proofreaders and editors for their thorough review and highly appreciated comments and suggestions, which significantly contributed to improving the quality of this manuscript.

REFERENCES

1. Newhauser WD, Zhang R. The physics of proton therapy. Phys Med Biol. 2015;60(8):155–209.
2. Ardenfors O, Dasu A, Lillhök J, Persson L, Gudowska I. Out-of-field doses from secondary radiation produced in proton therapy and the associated risk of radiation-induced cancer from a brain tumor treatment. Phys Med. 2018;53:129–136.
3. Paganetti H. Relative biological effectiveness (RBE) values for proton beam therapy. Variations as a function of biological endpoint, dose, and linear energy transfer. Phys Med Biol. 2014;59(22):419–472.
4. Eaton BR, MacDonald SM, Yock TI, Tarbell NJ. Secondary malignancy risk following proton radiation therapy. Front Oncol. 2015;5:261.
5. Upadhyay R, Yadav D, Venkatesulu BP, Singh R, Baliga S, Raval RR, et al. Risk of secondary malignant neoplasms in children following proton therapy vs. photon therapy for primary CNS tumors: A systematic review and meta-analysis. Front Oncol. 2022;12.
6. ICRP. The 2007 Recommendations of the International Commission on Radiological Protection. Ann ICRP. 2007;37(2-4):1–332.
7. Griffin KT, Yeom YS, Mille MM, Lee C, Jung JW, Hertel NE, et al. Comparison of out-of-field normal tissue dose estimates for pencil beam scanning proton therapy: MCNP6, PHITS, and TOPAS. Biomed Phys Eng Express. 2022;9(1).
8. Zheng Y, Liu Y, Zeidan O, Schreuder AN, Keole S. Measurements of neutron dose equivalent for a proton therapy center using uniform scanning proton beams. Med Phys. 2012;39(6):3484–3492.